coatings

MDPI

Article

Antibacterial Properties of PMMA Functionalized with $CuFe_2O_4/Cu_2O/CuO$ Nanoparticles

Elena Glazkova [1,*], Olga Bakina [1,*], Nikolay Rodkevich [1], Andrey Mosunov [2], Maxim Evstigneev [2], Vladislav Evstigneev [2], Viktor Klimenko [3] and Marat Lerner [1]

1 Institute of Strength Physics and Material Science, Siberian Branch of Russian Academy of Science, Av. Akademicheskii, 2/4, 634055 Tomsk, Russia; ngradk@ispms.tsc.ru (N.R.); lerner@ispms.tsc.ru (M.L.)
2 Laboratory of Molecular and Cellular Biophysics, Sevastopol State University, 33 Universitetskaya Street, 299053 Sevastopol, Russia; aamosunov@sevsu.ru (A.M.); max_evstigneev@mail.ru (M.E.); vald_e@rambler.ru (V.E.)
3 Center for Automotive and Road Engineering, Moscow Automobile and Road Construction State Technical University, Leningradsky Ave, 64, 125319 Moscow, Russia; klimenko@siberia.design
* Correspondence: eagl@ispms.tsc.ru (E.G.); ovbakina@ispms.tsc.ru (O.B.); Tel.: +7-(3822)-49-26-19 (O.B.)

Abstract: We have prepared a composite thin coating by incorporation of $CuFe_2O_4/Cu_2O/CuO$ nanoparticles in polymethyl methacrylate (PMMA) matrix by using the solution casting method. The electrical explosion of two twisted wires (EETW) was used to obtain multicomponent $CuFe_2O_4/Cu_2O/CuO$ nanoparticles with an average particle size of 20–70 nm. The microscopic studies showed that the nanoparticles in the composite coatings are evenly distributed. However, nanoparticles are strongly agglomerated as the powder concentration in the coating increases to 5 wt.% and 10 wt.%, as the size of particle agglomerates increases to 50 and 100 μm, respectively. Therefore, nanoparticles were pre-treated with ultrasound when introduced into the PMMA matrix. The thermal stability of the composite coating does not change with the introduction of $CuFe_2O_4/Cu_2O/CuO$ nanoparticles in the amount of 5 wt.%. The inclusion of nanoparticles in the PMMA matrix significantly enhances its antibacterial activity. The addition of 5 wt.% nanoparticles inhibited the growth of *E. coli* by 100% and the growth of MRSA by 99.94% compared to pure PMMA already after 3 h of exposure of bacteria on the surface of the composites. This research provides an easy-to-manufacture and cost-efficient method for producing a $CuFe_2O_4/Cu_2O/CuO$/PMMA composite coating with a broad application as an antibacterial material.

Keywords: polymethyl methacrylate; $CuFe_2O_4/Cu_2O/CuO$ nanoparticles; antibacterial coating; electrical explosion of two twisted wires

Citation: Glazkova, E.; Bakina, O.; Rodkevich, N.; Mosunov, A.; Evstigneev, M.; Evstigneev, V.; Klimenko, V.; Lerner, M. Antibacterial Properties of PMMA Functionalized with $CuFe_2O_4/Cu_2O/CuO$ Nanoparticles. *Coatings* **2022**, *12*, 957. https://doi.org/10.3390/coatings12070957

Academic Editor: Fengwei (David) Xie

Received: 17 May 2022
Accepted: 30 June 2022
Published: 6 July 2022

1. Introduction

Currently, polymethyl methacrylate (PMMA) is one of the most common polymer materials for biomedical applications [1]. The use of PMMA in medicine is primarily due to its good biocompatibility, physical and chemical stability, and affordability [2]. However, the polymer exhibits some drawbacks, such as a tendency to fatigue failure, low bending strength, low thermal stability, and the lack of the activity against microbial biofilm formation [3]. The biofouling tendency is related to the internal porosity of the PMMA base, which contributes to biofilm formation [4]. Although PMMA products have already shown promise in animal toxicity experiments [5], long-term use of such products is limited due to the occurrence of bacterial contamination [6]. In this regard, great attention is paid to the antibacterial and antifouling activity of PMMA products.

Several basic approaches (strategies) are commonly adopted to impart antibacterial properties to PMMA products, such as: the use of copolymers [7,8], the inclusion of antibiotics [6,9] or nanoparticles of both metals [10–12], as well as synthetic [13] and natural [14] polymers or ceramics [15,16]. Thus, the introduction of cationic polyethyleneimine led to a

chemical interaction with the polar acid groups of the bacterial wall [3] but caused the destruction of the polymeric matrix. The approach based on the introduction of antibacterial nanoparticles into the monomer prior to synthesis has a number of implications, ranging from changes in the nanoparticle sedimentation behavior and disperse composition to the influence on the polymer properties. Thus, antibacterial PMMA/silver nanoparticle (37–47 nm) nanocomposites have been obtained using an in situ radical polymerization technique [16]. However, the presence of Ag nanoparticles led to a decrease in the polymerization reaction rate and an increase in the average molecular weight of the resulting polymer. In this regard, the polymer surface modification is most preferable [17]. Currently, the search for non-toxic polymer modifiers is under way. The most promising direction is the use of photocatalysts, as they do not cause adverse biological and environmental effects [18]. However, due to the wide bandgap, the effective photocatalysts such as TiO_2 and ZnO show activity only in the UV region of the light spectrum [19].

A promising but insufficiently studied class of photocatalytic antibacterial agents are narrow-gap semiconductors—ferrite oxide compounds containing Fe^{3+} and another metal cation. Ferrites are characterized by absorption in the visible region, tunable optoelectronic properties, and high chemical and photochemical stability [20]. Recently, photocatalysts based on ferrite heterojunctions have been described. The $ZrO_2/ZnFe_2O_4$ nanocomposite provided a high degree of wastewater treatment under the sun irradiation due to the effective suppression of the charge carriers' recombination at the heterojunction [21]. The same mechanism explained the high photocatalytic activity of the $BiVO_4/ZnFe_2O_4$ composite [22]. Cobalt and zinc ferrites exhibited antibacterial activity under visible light irradiation due to photocatalytic generation of electron–hole pairs and reactive oxygen species (ROS), with the two-phase system with $CoFe_2O_4/ZnFe_2O_4$ contact being the most active [23]. Ce^{3+}-doped spinel $CuFe_2O_4$ nanoparticles exhibited antibacterial activity against *Klebsiella pneumoniae* and *Staphylococcus aureus* [24].

A non-toxic and promising reagent to generate ROS is copper ferrite $CuFe_2O_4$, which has attracted considerable research attention due to its thermal resistance and unique magnetic, electrical, magneto-optical, gas-sensitive, electrochemical, and catalytic properties. Compared with other catalysts, copper ferrites are the most environmentally friendly [25] and can find applications in medicine for the treatment of breast cancer [26]. The use of composite $CuO/CuFe_2O_4$ nanoparticles with a p-n heterojunction can improve the efficiency of the photocatalytic water decomposition reaction. The synthesis and studies of such systems have been actively pursued in recent years. $CuO/CuFe_2O_4$ nanocomposites exhibit conducting or semiconducting properties depending on the temperature, which has potential applications in various electronic devices, including sensors [27]. Thus, $CuO/CuFe_2O_4$ core-shell heterostructures have been used as sensors for hydrogen sulfide detection [28], but $CuO/CuFe_2O_4$ thin films as sensors for CO_2 [29], H_2, and C_2H_5OH detection [30]. The basic methods of ferrite synthesis are the sol-gel method, the co-precipitation method, the hydrothermal method, and solid-state reactions. Additionally, one can mention the combustion synthesis method used, for example, to produce copper ferrites, which consists in burning the solutions with L-arginine [31] and citric acid [32] as fuel. In this case, the formation of nanoparticles with a p-n heterojunction occurs at high temperatures in the vapor phase but is complicated by a number of chemical reactions with the formation of byproducts that contaminate the target product.

Considering the above-mentioned developments and their limitations, in the present work the electrical explosion of two twisted wires (EETW) was used to obtain multicomponent $CuFe_2O_4/Cu_2O/CuO$ nanoparticles. During EETW in an oxygen-containing atmosphere of iron wire together with copper, one of the phases formed is the corresponding ferrite with a spinel structure. The excess of the second metal forms the copper oxide phase (I, II). The ferrite and oxide phases are evenly distributed in the particle volume and separated by interphase boundaries, forming a p-n heterojunction. Moreover, the complex microstructure of $CuFe_2O_4/Cu_2O/CuO$ nanoparticles has several advantages, such as: (1) $CuFe_2O_4$ electrostatic interaction and complexing with phosphate in the cell wall [33],

(2) copper ions, Cu^{2+}, released from the samples would change the permeability of the bacterial cell wall, prevent the cell from absorbing nutrients, and ultimately affect the cell growth and vitality [34], and (3) iron (III) and copper ions can play a synergistic role in the antibacterial activity of nanoparticles [35]. Furthermore, the obtained $CuFe_2O_4/Cu_2O/CuO$ nanoparticles were encapsulated in PMMA film to afford it high antibacterial activity. To our knowledge, there have been no works on the application of $CuFe_2O_4/Cu_2O/CuO$ nanoparticles as antibacterial agents for PMMA modification.

2. Materials and Methods

2.1. Synthesis of $CuFe_2O_4/Cu_2O/CuO$ Nanoparticles

$CuFe_2O_4/Cu_2O/CuO$ nanoparticles (NPs) were obtained by electrical explosion of twisted copper and iron wires. A schematic diagram of the setup for producing NPs has been previously reported in [36]. Electrical explosion occurs when a high-current pulse generated by the discharge of an electric capacitor passes through the metal wire. Electrical explosion of Cu and Fe wires was carried out in a gas mixture containing 80 vol.% of argon and 20 vol.% of oxygen, with the Fe wire diameter being 0.30 mm, a Cu wire diameter of 0.20 mm, and a twisted wires' length of 90 mm. The electrical capacitance of the capacitor bank was 3.2 μF and the charge voltage was 28 kV. Under these conditions, the largest amount of copper ferrite is formed in the particles. The Cu:Fe atomic ratio in NPs was 50:50.

2.2. Synthesis of $CuFe_2O_4/Cu_2O/CuO/PMMA$ Composite Coating

Nanocomposite films with different contents of NPs (0.5 wt.%, 2 wt.%, 5 wt.%, and 10 wt.%) in the PMMA matrix were prepared by a solution casting method. In a typical procedure, 2.00 g of PMMA was dissolved in 10 mL of acetone at room temperature while stirring until a clear solution was obtained. Then, 0.01, 0.04, 0.1, or 0.2 g of $CuFe_2O_4/Cu_2O/CuO$ powder was added to the PMMA solution while stirring. The NPs-PMMA mixture was sonicated for 20 min to disperse and distribute NPs uniformly in the polymer solution. The final suspension was placed on a slide and left to dry at room temperature for 1 day for the physicochemical measurements and antimicrobial properties' determination.

2.3. Characterization

The morphology of NPs was characterized using scanning (SEM; LEO EVO 50, Zeiss, Oberkochen, Germany) and transmission electron microscopy (TEM; JEM 2100, JEOL, Tokyo, Japan). The elemental mapping in the NPs was carried out using an energy dispersive spectrometer (X-Max, Oxford Instruments, Abingdon, UK) integrated with a microscope. The phase composition of the NPs was determined using an XRD-6000 X-ray diffractometer (Shimadzu Corporation, Kyoto, Japan) using CuKα radiation (λ = 1.514 Å). Quantitative phase analysis of the NPs was carried out using the XPowder software package and the PDF2 database of crystallographic structures.

$CuFe_2O_4/Cu_2O/CuO/PMMA$ composite coatings were characterized using the AXIOVERT-200MAT optical microscope (Zeiss, Oberkochen, Germany). FT-IR absorption spectra were obtained using a Nicolet 5700 spectrometer (Thermo Electron, Waltham, MA, USA) in the 4000–400 cm^{-1} wavelength range. The thermal properties of coatings were studied in argon atmosphere using a TG-DSC instrument (STA449F3 Jupiter, Netzsch, Selb, Germany), a temperature range of 25–600 °C, and a heating rate of 10 °C/min. $CuFe_2O_4/Cu_2O/CuO/PMMA$ film surface wetting was measured at room temperature using a DSA100 optical goniometer (Krüss, Hamburg, Germany). A 5 μL droplet of deionized water was deposited on the surface of the film and the average value of the droplet contact angles in 5 different positions was obtained.

2.4. Antibacterial Activity of $CuFe_2O_4/Cu_2O/CuO/PMMA$ Composite Coatings

The antibacterial activities of nanocomposites were estimated using MRSA ATCC 43300 and *E. coli* ATCC 25922 bacterial strains. The antibacterial activity of the samples was

evaluated by the "drop contamination" method according to ISO 22196:2011, "Measurement of antibacterial activity on plastics and other non-porous surfaces". For this purpose, 5 × 5 cm composite plates were prepared. A volume of 400 µL of the bacterial suspension with a concentration of 10^5 CFU/mL was deposited on the surface of the samples and spread evenly over the surface using a spatula. The samples were covered with sterile polyethylene film and incubated for 1, 3, and 6 h at 37 °C and 100% relative humidity. After incubation, the samples were placed in containers with a neutralizer, a 0.9 wt.% NaCl solution, and thoroughly stirred. The solution was plated on Müller–Hinton agar (Thermo Fisher Scientific, Waltham, MA, USA) for MRSA and Endo agar (NICF, St. Petersburg, Russia). The number of grown colonies was evaluated after 24 h of incubation at 37 °C. For each sample, an antibacterial assay was performed with three independent replicates (n = 3).

3. Results and Discussion

3.1. Preparation and Physicochemical Characteristics of $CuFe_2O_4$/Cu_2O/CuO NPs

The following phases can form: CuO, Cu_2O, delafossite ($CuFeO_2$), spinel ($CuFe_2O_4$), during EETW of the two twisted iron and copper wires, based on the Cu-Fe-O phase diagram [37].

Figure 1 shows the XRD pattern of iron and copper oxide particles synthesized by EETW of copper and iron twisted wires in an oxygen-containing atmosphere. When the Fe/Cu atomic ratio equals 50:50, the phases $CuFe_2O_4$ with spinel structure and CuO with Cu_2O admixture are formed. The crystal structure of spinel is cubic face-centered packing formed by O^{2-} anions, and Cu^{2+} and Fe^{3+} cations are located in voids. The diffraction peaks in Figure 2 at 2θ angles around 30.15°, 35.52°, 43.18°, 53.60°, 57.12°, 62.73°, and 74.25° are identified as the (220), (311), (400), (422), (511), and (440) planes of the cubic spinel structure $CuFe_2O_4$, respectively. This is confirmed by the data provided in [38,39]. Diffraction peaks at 2θ angles of 36°, 42.5°, and 74° are attributed to crystal planes of Cu_2O, and peaks at 39° and 71° were indexed to be CuO. The Reference Intensity Ratio (RIR) method was used for quantitative analysis by powder diffraction. The mass ratio of copper ferrite phase was 72.4 wt.%, and of copper oxide (I) and (II) was 20.5 and 7.1 wt.%, respectively.

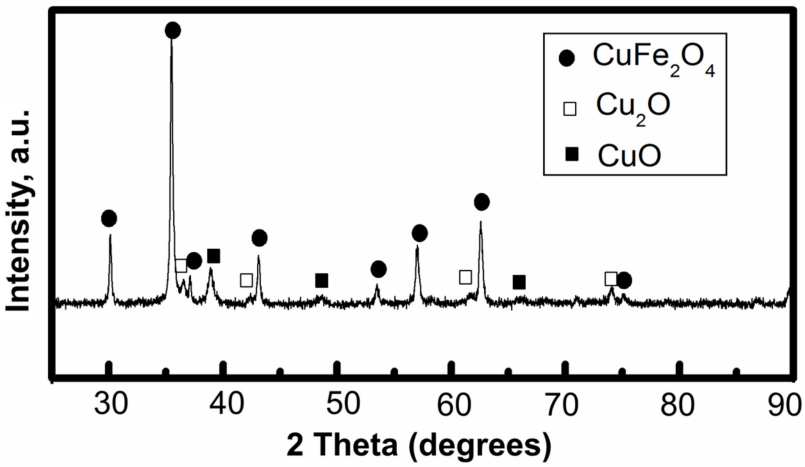

Figure 1. XRD pattern of $CuFe_2O_4$/Cu_2O/CuO NPs.

TEM and SEM images of NPs are presented in Figure 2. It was clearly seen that NPs are mostly spherical in shape.

According to SEM data (Figure 2a), large agglomerates up to 1 µm in size are found in all samples. The NPs have a close to spherical shape (Figure 2b), and the particle size ranges from 10 to 100 nm. The smaller NPs are somewhat faceted. Detailed elemental mapping studies showed that Cu, Fe, and O are evenly distributed in the NPs.

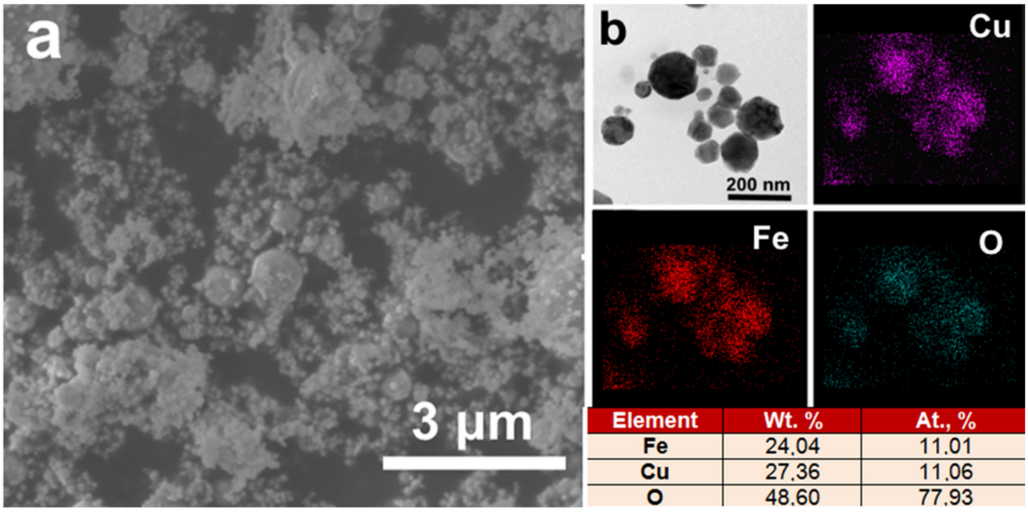

Figure 2. SEM image of $CuFe_2O_4/Cu_2O/CuO$ NPs (**a**) and TEM and EDX mapping showing copper, iron, and oxygen distribution in NPs (**b**).

One of the main problems in the introduction of nanoparticles into polymeric matrices is their agglomeration [40]. The high surface area of nanoparticles and the strong attractive van der Waals interaction between them result in the agglomeration. In various processes, nanoparticle agglomerates behave as a separate large particle [41]. This is determined by the fact that nanoparticle agglomerates have a much smaller contact surface area with the external environment relative to individual nanoparticles, which reduces the advantages of nanoparticle applications. The full potential of nanoparticles can be achieved only by breaking down nanoparticle aggregates, preferably to primary particles. Silver nanoparticles used in the present study formed agglomerates, which was confirmed by the sedimentation analysis data. The particle size study by the density gradient sedimentation method showed a bimodal distribution in size regardless of the phase composition, with the peak maxima being at 30–50 and 100–200 nm. Considering the results of the TEM analysis, the first peak appears to show the distribution of NPs, while the second results from both nanoparticles and NP agglomerates. The peak in the distribution is shifted toward particles of 20–70 nm in size. The specific surface area of the sample was 12.9 ± 1.2 m^2/g. The agglomeration of nanoparticles leads to a decrease in antibacterial activity, as shown in [42]. However, it was not possible to fully break down the nanoparticle agglomerates by ultrasonic treatment. A further increase in the dispersion time leads to local heating and sintering of nanoparticles.

3.2. Characterization of $CuFe_2O_4/Cu_2O/CuO$/PMMA Composites

Optical microscopic images of $CuFe_2O_4/Cu_2O/CuO$/PMMA films are shown in Figure 3.

The microscopic studies showed that the $CuFe_2O_4/Cu_2O/CuO$ NPs in the composite coatings are evenly distributed. However, they are strongly agglomerated, and the size of NP agglomerates increases. Therefore, NP suspension was treated with ultrasound when introduced into the PMMA matrix. The 0.5 wt.% and 2 wt.% NP composite samples included both particles and particle agglomerates up to 20 μm in size, uniformly distributed in the PMMA matrix. The 5 and 10 wt.% NP composite samples also show a uniform distribution of the particle agglomerates in the PMMA matrix, but the size of the agglomerates increases significantly to 50 μm and over 100 μm, respectively.

Figure 4 displays the FT-IR spectra of NPs and composites doped with 5 wt.% of NPs.

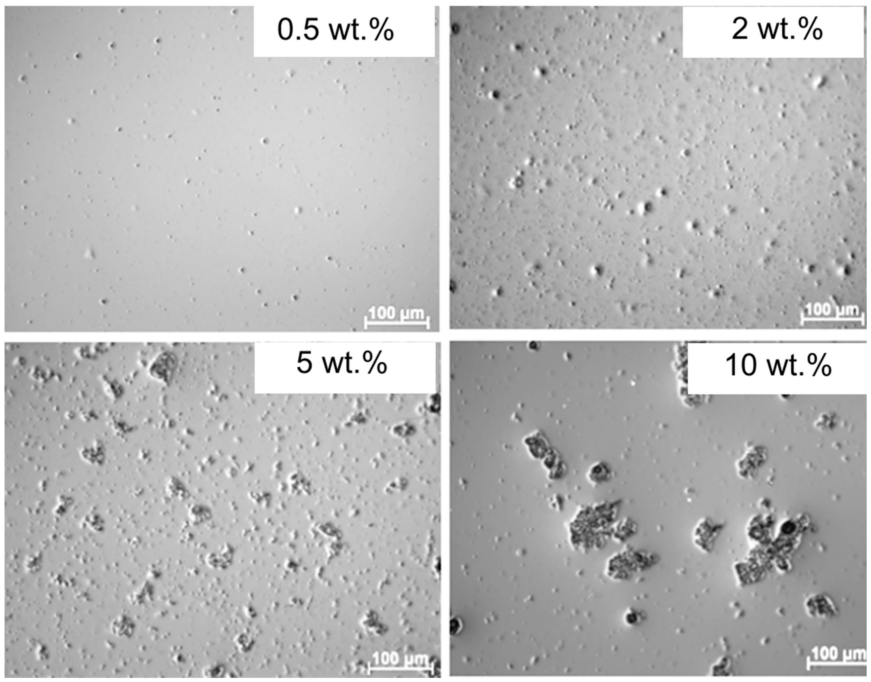

Figure 3. Optical microscopy of $CuFe_2O_4/Cu_2O/CuO$ composite coatings as a function of the NP content.

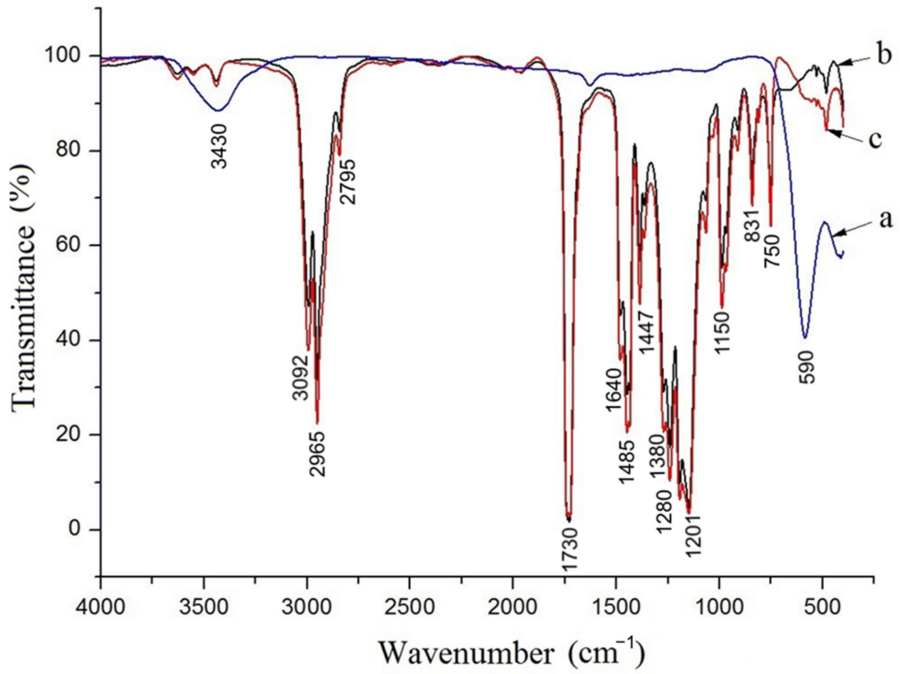

Figure 4. FT-IR spectra of: (**a**) NPs, (**b**) 5 wt.% NP composite, and (**c**) clear PMMA.

Figure 4a shows the FT-IR spectrum of NPs. The band at 590 cm^{-1} is related to Fe^{3+}–O^{2-} stretching of tetrahedral complexes [43]. The bands at 3430 and 1640 cm^{-1} correspond to O–H stretching of adsorbed H_2O. The FT-IR spectrum of PMMA (Figure 4b) contains bands located at 2750–3100 cm^{-1}, which are attributed to asymmetric and symmetric stretching of the CH_3 group. The band at 1730 cm^{-1} is related to the C=O stretching of carboxyl PMMA [44]. The bands at 1485, 1447, and 1380 cm^{-1} are attributed to CH_3 deformation. Bends located at 1280–1150 cm^{-1} are assigned to the stretching or the frequency of the ester group (C–O–C). Absorption peaks at 985 and 960 cm^{-1} correspond to

C-C symmetric stretching. The bands at 831 and 750 cm^{-1} are related to -CH_2 asymmetric rocking and -CH_2 rocking [45–47]. The FT-IR spectrum of the composite (Figure 4c) contains bands attributed to PMMA and NPs and did not show any new peaks. This indicates that PMMA and NPs are only physically blended.

The authors of [48] noted hydrophobicity to be a dominant factor in influencing adhesion on surfaces. Bacteria with hydrophilic properties (*E. coli*, MRSA) prefer to adhere to hydrophilic surfaces. For example, *S. aureus* (including MRSA) has a hydrophilic character, which favors the adhesion of this bacterium to metal alloys over ultra-high molecular weight polyethylene that present a more hydrophobic surface. The hydrophilicity of the coatings was evaluated by measuring the water contact angle (Figure 5).

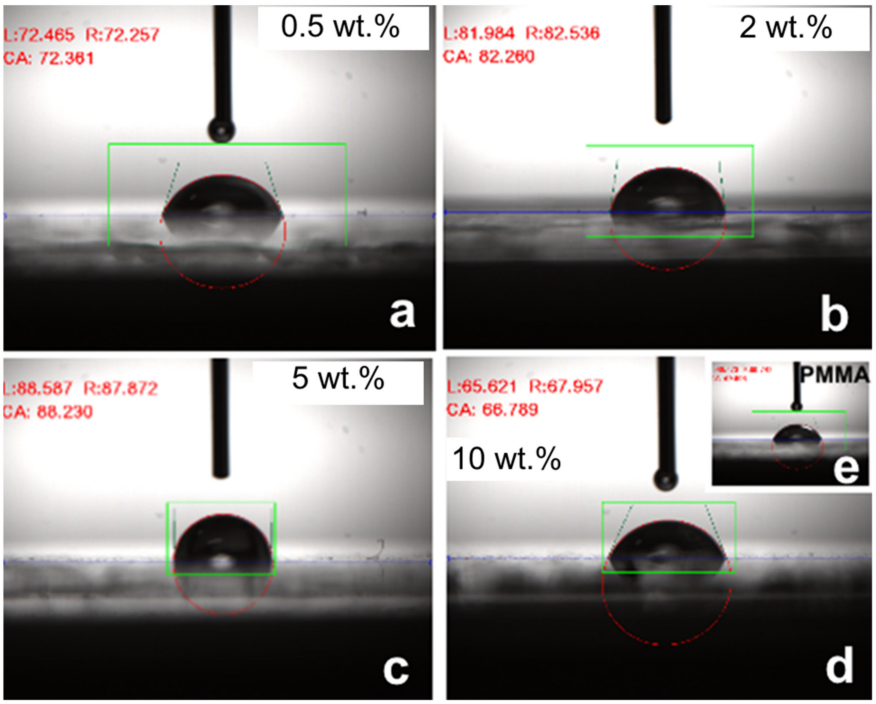

Figure 5. Water contact angle of NP composite with 0.5 wt.% (**a**), 2 wt.% (**b**), 5 wt.% (**c**), 10 wt.% (**d**), and clear PMMA (**e**).

The water contact angle of the PMMA coating was 69.66° ± 1.1°. Adding NPs at 0.5, 1, and 5 wt.% increased the contact angle, indicating reduced PMMA surface wettability. As the content of the NPs in the composite increased to 5 wt.%, the contact angles of the deionized water increased to 86.33° + 5.75°. This can be attributed to an increase in surface tension by the hydrophobic $CuFe_2O_4/Cu_2O/CuO$ nanoparticles. When 10 wt.% of NPs was added in PMMA, the contact angle for the composite was 66.5° ± 2.8°, significantly lower than that for pure PMMA. This decrease in the contact angle reflects a reduction in surface hydrophobicity, which could be caused by a reduction in the total surface area of the nanoparticles due to their agglomeration.

To evaluate the thermal stability of the $CuFe_2O_4/Cu_2O/CuO$/PMMA composite coating, the thermogravimetric measurements of PMMA and the composite coatings containing 0.5 wt.% to 5 wt.% NPs were performed.

Respective plots of the samples are shown in Figure 6. As seen in Figure 6, the weight loss occurs in two stages. The first stage is observed in the temperature range of 150–190 °C, with a weight loss of 3.3%–7.3%. This is due to the destruction of part of the polymer. The second stage of weight loss occurs between 360 and 390 °C and amounts to 85.4%–96.8%, which is associated with the thermal degradation of the polymer. The kinetics of the second stage of mass loss is almost the same for all samples, which indicates that the destruction mechanism and thermal stability of the composites is not changed significantly as compared

to the PMMA polymer. TG curves can be represented as a set of sigmoid curves, each describing a different stage of the chemical process. To evaluate TG thermal parameters, a fitting model of the sample mass as a function of temperature can be represented in the form [49]:

$$M(T) = \sum_{i=1}^{N} \frac{M_i}{(1 + \tau_i \exp(b_i(T - \theta_i))^{1/\tau_i}} \quad (1)$$

where *M(T)* is the sample mass at temperature *T*, *N* is the number of sigmoid components, i.e., the number of process stages, *T* is the temperature, M_i is the magnitude of the mass sample reacted at each stage, b_i is the rate parameter of mass change, θ_i is the temperature of the maximum rate of mass change at each stage, and τ_i is the asymmetry parameter of each stage. As the value of τ increases, the slope of the curve decreases, which means that the rate of the process decreases.

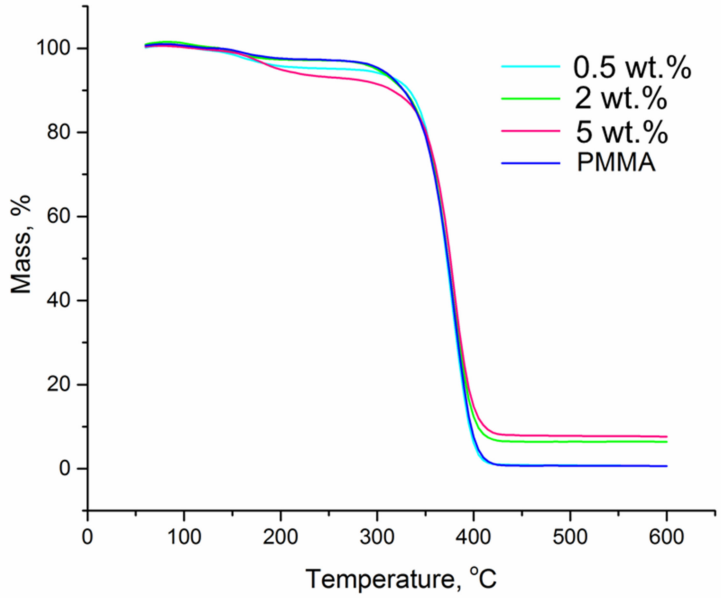

Figure 6. TG curves of PMMA and $CuFe_2O_4/Cu_2O/CuO$/PMMA composites containing 0.5, 2, and 5 wt.% NPs.

Fitted thermal parameters are listed in Table 1.

Table 1. Fitted TG thermal parameters.

Sample		PMMA	0.5 wt.% NPs	2 wt.% NPs	5 wt.% NPs
Stage I	M	5.70	4.96	5.33	10.71
	θ	156.	150	154	173
	b^1	18.20	9.65	16.7	16.2
	τ	1.72	3.58	4.41	5.12
Stage II	M	94.10	94.90	88.30	82.07
	θ	377.00	378	378	378
	b	15.1	17.89	16.48	13.60
	τ	0.11	0.10	0.27	0.49
	R^2	0.9999	0.9999	0.9999	0.9999

As can be concluded from the presented data, the destruction of PMMA occurs in two stages. The effect of the introduced ferrite nanoparticles on the process of PMMA destruction in the first stage is evident only at a ferrite nanoparticle content of more than

2 wt.%, which results from the increase in the temperature of the maximum destruction rate and the increase in the mass fraction of the polymer subjected to destruction. Additionally, with the increasing ferrite nanoparticle content in the composite, the asymmetry parameter slightly increases, which may be related to the deceleration of PMMA nanoparticles at a higher temperature with the formation of volatile products. In the second stage of the PMMA destruction process, the effect of injected ferrite nanoparticles is less noticeable. The temperature of the maximum destruction rate is almost constant, but the mass fraction of the polymer subjected to destruction is lower. The overall rate of the degradation process decreases with the increasing ferrite nanoparticle content in the composite, and from the increase in the asymmetry parameter it can be concluded that the process of PMMA destruction with the formation of nonvolatile products (carbonization) dominates over the process of PMMA destruction with the formation of volatile products. Thus, it can be concluded that the first stage of composite destruction is dominated by PMMA destruction with the formation of volatile products, while the second stage of the destruction is dominated by the process with the formation of nonvolatile products. The residual amount of degradation products of composites increases from 0.4% to 7% with the increasing nanoparticle content in the composite. The increased content of degradation products for the 2 wt. % and 5 wt.% NP composite samples, respectively, 6% and 7%, is probably due to the fact that polymer carbonization occurs in the presence of NPs. Thus, the thermal stability of the composite coating does not change with the introduction of NPs in the amount from 0.5 wt.% to 5 wt.%.

3.3. Antibacterial Activity of Composites

The antibacterial activity of the $CuFe_2O_4/Cu_2O/CuO$/PMMA composites was evaluated by the inactivation of MRSA and *E. coli* bacteria deposited on the composite surface. The samples containing 5 wt.% and 10 wt.% NPs showed a significant bacterial reduction against MRSA (Figure 7) and *E. coli* (Figure 8) compared to pure PMMA. The bacteria reduction as a function of the amounts of nanoparticles after 3 h of exposure is shown in Figures 7a and 8a.

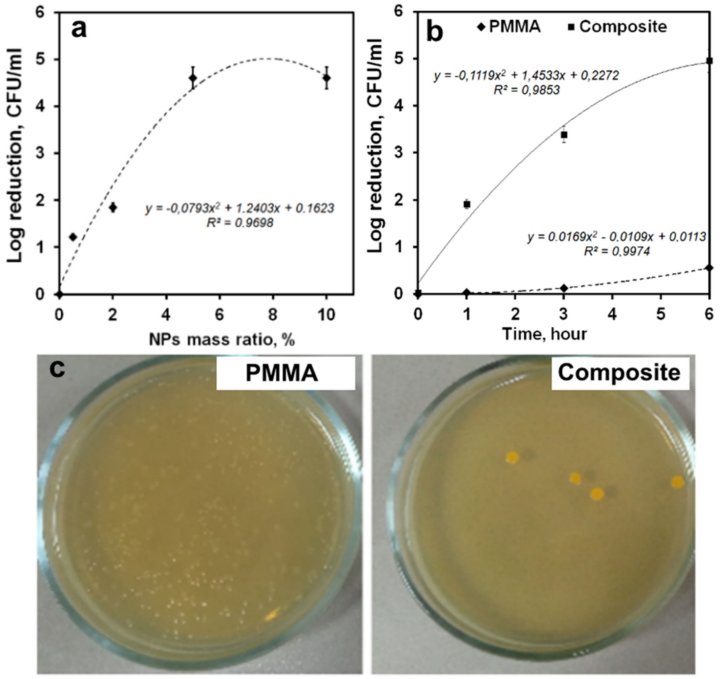

Figure 7. MRSA log reduction after exposure on the surface of the composites with different NP mass ratios (**a**). Time-dependent MRSA log reduction after exposure on the surface of the PMMA and composite, containing 5 wt.% NPs (**b**). Photographs of typical Petri dishes after 3 h exposure of MRSA on the surface of the PMMA and composite, containing 5 wt.% NPs (**c**).

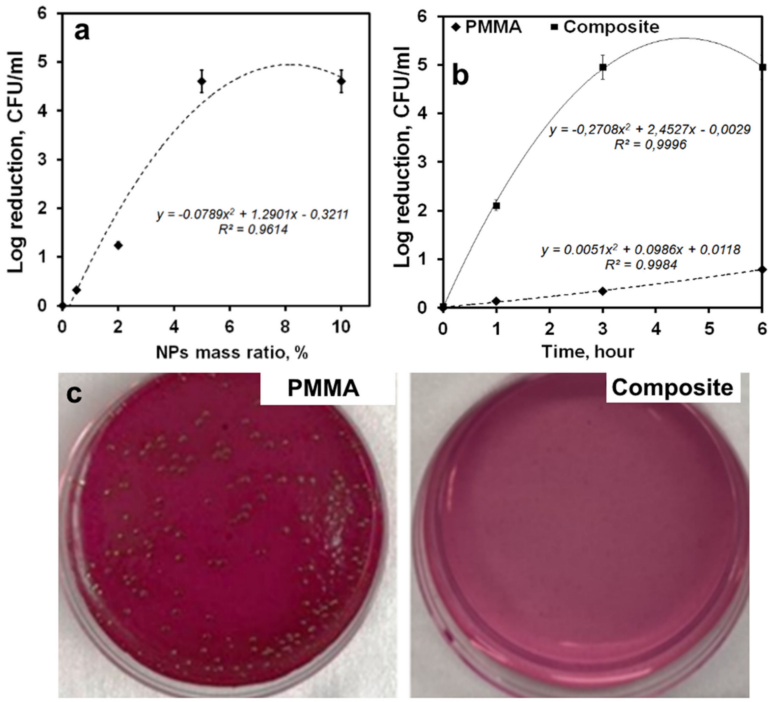

Figure 8. *E. coli* log reduction after exposure on the surface of the composites with different NP mass ratios (**a**). Time-dependent *E. coli* log reduction after exposure on the surface of the PMMA and composite, containing 5 wt.% NPs (**b**). Photographs of typical Petri dishes after 3 h exposure of *E. coli* on the surface of the PMMA and composite, containing 5 wt.% NPs (**c**).

As can be seen, the inclusion of nanoparticles in the PMMA matrix significantly enhances its antibacterial activity, especially with the addition of 5 wt.% NPs or more (Table 2). The addition of 5 wt.% NPs inhibited the growth of *E. coli* by 100% and the growth of MRSA by 99.94% already after 3 h of exposure of bacteria on the surface of the composites.

Table 2. Antibacterial activity of the samples.

Sample	Colony-Forming Unit, CFU/mL			R *, %		
	1 h	3 h	6 h	1 h	3 h	6 h
			E. coli			
PMMA	$6.63 \times 10^4 \pm 0.45 \times 10^4$	$4.10 \times 10^4 \pm 0.06 \times 10^4$	$1.47 \times 10^4 \pm 0.12 \times 10^4$	33.7	59.0	85.3
0.5 wt.%	$2.67 \times 10^4 \pm 0.12 \times 10^4$	$1.9 \times 10^4 \pm 0.1 \times 10^4$	$1.30 \times 10^3 \pm 0.02 \times 10^3$	73.3	81.0	98.7
2 wt.%	$1.03 \times 10^4 \pm 0.12 \times 10^4$	$0.23 \times 10^4 \pm 0.06 \times 10^4$	$0.10 \times 10^3 \pm 0.00 \times 10^3$	89.7	97.7	99.9
5 wt.%	$0.70 \times 10^3 \pm 0.12 \times 10^3$	0 ± 0	0 ± 0	99.3	100	100
10 wt.%	$5.17 \times 10^2 \pm 0.12 \times 10^2$	0 ± 0	0 ± 0	99.5	100	100
			MRSA			
PMMA	$8.33 \times 10^4 \pm 0.40 \times 10^4$	$6.83 \times 10^4 \pm 0.11 \times 10^4$	$2.50 \times 10^4 \pm 0.09 \times 10^4$	16.7	31.7	75.0
0.5 wt.%	$9.20 \times 10^3 \pm 0.50 \times 10^3$	$2.40 \times 10^3 \pm 0.40 \times 10^3$	$0.33 \times 10^3 \pm 0.05 \times 10^3$	90.8	97.6	99.7
2 wt.%	$2.33 \times 10^3 \pm 0.31 \times 10^3$	$5.70 \times 10^2 \pm 0.05 \times 10^2$	$0.87 \times 10^2 \pm 0.08 \times 10^2$	97.7	99.4	99.9
5 wt.%	$1.10 \times 10^3 \pm 0.04 \times 10^3$	39.67 ± 1.52	0 ± 0	98.9	99.9	100
10 wt.%	$5.17 \times 10^2 \pm 0.12 \times 10^2$	0 ± 0	0 ± 0	99.5	100	100

* The antibacterial activity (R %) was expressed as the % reduction of the number of cells, which was calculated using the formula: $R = (C_0 - C)/C_0$, where C_0 is the number of viable bacteria recovered from the control (10^5 CFU/mL) and C is the number of viable bacteria in CFU/mL recovered from experimental samples.

PMMA used as a control had practically no effect on the viability of the microorganisms studied. These results are consistent with earlier experiments on the modification of PMMA with silver nanoparticles [46], copper oxide [50], and titania nanoparticles [51]. As shown in [52], the modification of cationic polyethyleneimine/anionic pectin hydrogel with polydopamine Cu nanoparticles reduced survival rates for *S. aureus* from 80.2% to 34.6%, and for *E. coli* from 71.1% to 22.4%. Antibacterial activity of $CuFe_2O_4/Cu_2O/CuO$/PMMA composites against *E. coli* is higher than that against *S. aureus* (Figure 7b). It can be ascribed to the differences in the membrane structure and composition of these bacteria. *E. coli* has a complicated cell wall with internal and thin external membranes composed of peptidoglycan, lipopolysaccharides, lipoproteins, and phospholipids molecules. The *S. aureus* cell wall has a single thick membrane of peptidoglycan. Therefore, *E. coli* is more impressible for penetrating antibacterial agents [53]. The antibacterial effect of the $CuFe_2O_4/Cu_2O/CuO$/PMMA composite may be described using three mechanisms: (1) effective interaction of the nanoparticle with the bacterial cell wall due to its high surface-to-volume ratio, (2) release of copper ions, which had a destructive effect on the structures of bacteria cells' membranes, and (3) their capability to produce reactive oxygen species (ROS). According to [54], the main mechanism of the ferrite nanoparticle action is based on ROS generation. ROS generation causes lipid peroxidation, destruction or modification of proteins, violation of the integrity of the bacterial membrane, destruction of enzymes, and RNA damage, leading to cell death.

4. Conclusions

In this study, we developed novel $CuFe_2O_4/Cu_2O/CuO$/polymethyl methacrylate PMMA coatings and analyzed their antibacterial performance. The electrical explosion of two twisted wires was used to obtain multicomponent $CuFe_2O_4/Cu_2O/CuO$ nanoparticles. The microscopic studies showed that the nanoparticles in the composite coatings were evenly distributed. The inclusion of nanoparticles in the PMMA matrix significantly enhanced its antibacterial activity. The addition of 5 wt.% nanoparticles inhibited the growth of *E. coli* by 100% and the growth of MRSA by 99.94% already after 3 h of exposure of bacteria on the surface of the composites. Thus, the active antibacterial composite thin coatings can control bacterial biofilm formation, which could resist the attachment and growth of fouling microorganisms.

Author Contributions: Conceptualization, E.G., M.L. and O.B.; methodology and validation, N.R.; investigation, E.G. and O.B.; data curation, V.K.; writing—original draft, E.G., O.B. and A.M.; writing—review and editing, V.E. and M.E.; supervision, M.L. All authors have read and agreed to the published version of the manuscript.

Funding: This research was funded by the Russian Science Foundation (Project No. 21-13-00498).

Institutional Review Board Statement: Not applicable.

Informed Consent Statement: Not applicable.

Data Availability Statement: Not applicable.

Conflicts of Interest: The authors declare no conflict of interest.

References

1. Ali, U.; Karim, K.J.B.A.; Buang, N.A. A review of the properties and applications of poly (methyl methacrylate) (PMMA). *Polym. Rev.* **2015**, *55*, 678–705. [CrossRef]
2. Frazer, R.Q.; Byron, R.T.; Osborne, P.B.; West, K.P. PMMA: An essential material in medicine and dentistry. *J. Long-Term Eff. Med. Implant.* **2005**, *15*, 629–639. [CrossRef] [PubMed]
3. Karatepe, U.Y.; Ozdemir, T. Improving mechanical and antibacterial properties of PMMA via polyblend electrospinning with silk fibroin and polyethyleneimine towards dental applications. *Bioact. Mater.* **2020**, *5*, 510–515. [CrossRef] [PubMed]
4. Hadjiev, D.; Dimitrov, D.; Martinov, M.; Sire, O. Enhancement of the biofilm formation on polymeric supports by surface conditioning. *Enzym. Microb. Technol.* **2007**, *40*, 840–848. [CrossRef]

5. Fottner, A.; Nies, B.; Kitanovic, D.; Steinbrück, A.; Hausdorf, J.; Mayer-Wagner, S.; Jansson, V. In vivo evaluation of bioactive PMMA-based bone cement with unchanged mechanical properties in a load-bearing model on rabbits. *J. Biomater. Appl.* **2015**, *30*, 30–37. [CrossRef]
6. Van Vugt, T.A.; Arts, J.J.; Geurts, J.A. Antibiotic-loaded polymethylmethacrylate beads and spacers in treatment of orthopedic infections and the role of biofilm formation. *Front. Microbiol.* **2019**, *10*, 1626. [CrossRef]
7. Sh, R.N.; Azizov, A.H.; Ibadov, E.A.; Zaynalova, S.G.; Sh, R.N. The research of antibacterial properties of methyl methacrylate and methacryloyl salicylate copolymers. *Azerbaijan Chem. J.* **2017**, *3*, 17–19.
8. Sun, X.; Qian, Z.; Luo, L.; Yuan, Q.; Guo, X.; Tao, L.; Wang, X. Antibacterial adhesion of poly (methyl methacrylate) modified by borneol acrylate. *ACS Appl. Mater. Interfaces* **2016**, *8*, 28522–28528. [CrossRef]
9. Patel, S.R.; Ramanujam, C.L.; Zgonis, T. A Guide to Using Antibiotic-Loaded PMMA Beads and Spacers in the Diabetic Foot. *Diabet. Foot* **2019**, *32*, 5. Available online: https://www.hmpgloballearningnetwork.com/site/podiatry/guide-using-antibiotic-loaded-pmma-beads-and-spacers-diabetic-foot (accessed on 16 May 2022).
10. Nam, K.Y. Characterization and antifungal activity of the modified PMMA denture base acrylic: Nanocomposites impregnated with gold, platinum, and silver nanoparticles. In *Nanobiomaterials in Dentistry*; William Andrew Publishing: Norwich, NY, USA, 2016; pp. 309–336.
11. Sathya, S.; Murthy, P.S.; Das, A.; Sankar, G.G.; Venkatnarayanan, S.; Pandian, R.; Venugopalan, V.P. Marine antifouling property of PMMA nanocomposite films: Results of laboratory and field assessment. *Int. Biodeterior. Biodegrad.* **2016**, *114*, 57–66. [CrossRef]
12. Yang, D.H.; Yoon, G.H.; Shin, G.J.; Kim, S.H.; Rhee, J.M.; Khang, G.; Lee, H.B. Surface and chemical properties of surface-modified UHMWPE powder and mechanical and thermal properties of its impregnated PMMA bone cement V. Effect of silane coupling agent on the surface modification of UHMWPE powder. *Macromol. Res.* **2005**, *13*, 120–127. [CrossRef]
13. Shi, Z.; Neoh, K.G.; Kang, E.T.; Wang, W. Antibacterial and mechanical properties of bone cement impregnated with chitosan nanoparticles. *Biomaterials* **2006**, *27*, 2440–2449. [CrossRef] [PubMed]
14. Zidan, S.; Silikas, N.; Alhotan, A.; Haider, J.; Yates, J. Investigating the mechanical properties of ZrO_2-impregnated PMMA nanocomposite for denture-based applications. *Materials* **2019**, *12*, 1344. [CrossRef] [PubMed]
15. Zidan, S.; Silikas, N.; Haider, J.; Alhotan, A.; Jahantigh, J.; Yates, J. Assessing Tensile bond strength between denture teeth and nano-zirconia impregnated PMMA denture base. *Int. J. Nanomed.* **2020**, *15*, 9611. [CrossRef]
16. Siddiqui, M.N.; Redhwi, H.H.; Vakalopoulou, E.; Tsagkalias, I.; Ioannidou, M.D.; Achilias, D.S. Synthesis, characterization and reaction kinetics of PMMA/silver nanocomposites prepared via in situ radical polymerization. *Eur. Polym. J.* **2015**, *72*, 256–269. [CrossRef]
17. Wentao, W.; Tao, Z.; Bulei, S.; Tongchang, Z.; Qicheng, Z.; Fan, W.; Yi, S. Functionalization of polyvinyl alcohol composite film wrapped in am-ZnO@CuO@Au nanoparticles for antibacterial application and wound healing. *Appl. Mater. Today* **2019**, *17*, 36–44. [CrossRef]
18. Zhou, Z.; Li, B.; Liu, X.; Li, Z.; Zhu, S.; Liang, Y.; Wu, S. Recent progress in photocatalytic antibacterial. *ACS Appl. Bio Mater.* **2021**, *4*, 3909–3936. [CrossRef]
19. Sodagar, A.; Khalil, S.; Kassaee, M.Z.; Shahroudi, A.S.; Pourakbari, B.; Bahador, A. Antimicrobial properties of poly (methyl methacrylate) acrylic resins incorporated with silicon dioxide and titanium dioxide nanoparticles on cariogenic bacteria. *J. Orthod. Sci.* **2016**, *5*, 7. [CrossRef]
20. Garcia-Muñoz, P.; Fresno, F.; Peña O'Shea, V.A.; Keller, N. Ferrite materials for photoassisted environmental and solar fuels applications. *Heterog. Photocatal.* **2020**, *378*, 107–162. [CrossRef]
21. Renuka, L.; Anantharaju, K.S.; Vidya, Y.S.; Nagabhushana, H.; Uma, B.; Malini, S.; Koppad, P. Porous network $ZrO_2/ZnFe_2O_4$ nanocomposite with heterojunction towards industrial water purification under sunlight: Enhanced charge separation and elucidation of photo-mechanism. *Ceram. Int.* **2021**, *47*, 14845–14861. [CrossRef]
22. Ma, A.; Gao, Y.; Zhang, D.; Hou, X. Use of m-$BiVO_4/ZnFe_2O_4$ composite materials for enhanced photocatalytic properties. *Surf. Innov.* **2020**, *9*, 139–148. [CrossRef]
23. Ramadan, R.; Ahmed, M.K.; Uskoković, V. Magnetic, microstructural and photoactivated antibacterial features of nanostructured Co–Zn ferrites of different chemical and phase compositions. *J. Alloys Compd.* **2021**, *856*, 157013. [CrossRef]
24. Elayakumar, K.; Manikandan, A.; Dinesh, A.; Thanrasu, K.; Raja, K.K.; Kumar, R.T.; Baykal, A. Enhanced magnetic property and antibacterial biomedical activity of Ce^{3+} doped CuFe2O4 spinel nanoparticles synthesized by sol-gel method. *J. Magn. Magn. Mater.* **2019**, *478*, 140–147. [CrossRef]
25. Akbar Hosseini, S. Low-cost and eco-friendly viable approach for synthesis of thulium doped copper ferrite nanoparticles using starch. *J. Mater. Sci. Mater. Electron.* **2016**, *27*, 7433–7437. [CrossRef]
26. Masunga, N.; Mmelesi, O.K.; Kefeni, K.K.; Mamba, B.B. Recent advances in copper ferrite nanoparticles and nanocomposites synthesis, magnetic properties and application in water treatment. *J. Environ. Chem. Eng.* **2019**, *7*, 103179. [CrossRef]
27. Özdemir, Z.G.; Kılıç, M.; Karabul, Y.; Mısırlıoğlu, B.S.; Çakır, Ö.; Kahya, N.D. A transition in the electrical conduction mechanism of $CuO/CuFe_2O_4$ nanocomposites. *J. Electroceramics* **2020**, *44*, 1–15. [CrossRef]
28. Boepple, M.; Zhu, Z.; Hu, X.; Weimar, U.; Barsan, N. Impact of heterostructures on hydrogen sulfide sensing: Example of core-shell $CuO/CuFe_2O_4$ nanostructures. *Sens. Actuators B Chem.* **2020**, *321*, 128523. [CrossRef]
29. Chapelle, A.; El Younsi, I.; Vitale, S.; Thimont, Y.; Nelis, T.; Presmanes, L.; Tailhades, P. Improved semiconducting $CuO/CuFe_2O_4$ nanostructured thin films for CO_2 gas sensing. *Sens. Actuators B Chem.* **2014**, *204*, 407–413. [CrossRef]

30. De, S.; Venkataramani, N.; Prasad, S.; Dusane, R.O.; Presmanes, L.; Thimont, Y.; Barnabé, A. Ethanol and hydrogen gas-sensing properties of CuO–$CuFe_2O_4$ nanostructured thin films. *IEEE Sens. J.* **2018**, *18*, 6937–6945. [CrossRef]
31. Dhiwahar, A.T.; Maruthamuthu, S.; Marnadu, R.; Sundararajan, M.; Manthrammel, M.A.; Shkir, M.; Reddy, V.R.M. Improved photocatalytic degradation of rhodamine B under visible light and magnetic properties using microwave combustion grown Ni doped copper ferrite spinel nanoparticles. *Solid State Sci.* **2021**, *113*, 106542. [CrossRef]
32. Liu, J.M.; Lu, Y.H.; Xu, Z.F.; Wang, R.X.; Yan, H.C.; Li, X. Effect of citric acid-to-nitrate ratio on combustion synthesis of $CuFe_2O_4$ for sodium-ion storage. *J. Mater. Sci. Mater. Electron.* **2021**, *32*, 94–101. [CrossRef]
33. Zhang, Y.; Chen, Y.; Kang, Z.V.; Gao, X.; Zeng, X.; Liu, M.; Yang, D.P. Waste eggshell membrane-assisted synthesis of magnetic $CuFe_2O_4$ nanomaterials with multifunctional properties (adsorptive, catalytic, antibacterial) for water remediation. *Colloids Surf. A Physicochem. Eng. Asp.* **2021**, *612*, 125874. [CrossRef]
34. Li, Q.; Yong, C.; Cao, W.; Wang, X.; Wang, L.; Zhou, J.; Xing, X. Fabrication of charge reversible graphene oxide-based nanocomposite with multiple antibacterial modes and magnetic recyclability. *J. Colloid Interface Sci.* **2018**, *511*, 285–295. [CrossRef]
35. Bakina, O.V.; Glazkova, E.A.; Svarovskaya, N.V.; Rodkevich, N.G.; Lerner, M.I. «Janus»-like Cu-Fe bimetallic nanoparticles with high antibacterial activity. *Mater. Lett.* **2019**, *242*, 187–190. [CrossRef]
36. Lerner, M.I.; Pervikov, A.V.; Glazkova, E.A.; Svarovskaya, N.V.; Lozhkomoev, A.S.; Psakhie, S.G. Structures of binary metallic nanoparticles produced by electrical explosion of two wires from immiscible elements. *Powder Technol.* **2016**, *288*, 371–378. [CrossRef]
37. Schorne-Pinto, J.; Cassayre, L.; Presmanes, L.; Barnabé, A. Insights on the stability and cationic nonstoichiometry of $CuFeO_2$ delafossite. *Inorg. Chem.* **2019**, *58*, 6431–6444. [CrossRef] [PubMed]
38. Atacan, K. $CuFe_2O_4$/reduced graphene oxide nanocomposite decorated with gold nanoparticles as a new electrochemical sensor material for L-cysteine detection. *J. Alloys Compd.* **2019**, *791*, 391–401. [CrossRef]
39. Thakare, P.S.; Padole, P.R.; Bodade, A.B.; Chaudhari, G.N. Microstructural and Antifungal Properties of Silver Substituted Copper Ferrite Nanopowder Synthesized By Sol-Gel Method. *Indo Am. J. Pharm. Sci.* **2018**, *5*, 52–63. [CrossRef]
40. Svarovskaya, N.V.; Bakina, O.V.; Pervikov, A.V.; Rubtsov, K.V.; Lerner, M.I. Electrical Explosion of Wires for Manufacturing Bimetallic Antibacterial Ti-Ag and Fe-Ag Nanoparticles. *Russ. Phys. J.* **2020**, *62*, 1580–1586. [CrossRef]
41. Deng, X.; Huang, Z.; Wang, W.; Davé, R.N. Investigation of nanoparticle agglomerates properties using Monte Carlo simulations. *Adv. Pow. Technol.* **2016**, *27*, 1971–1979. [CrossRef]
42. Holubnycha, V.; Myronov, P.; Bugaiov, V.; Opanasyuk, A.; Dobrozhan, O.; Yanovska, A.; Pogorielov, M.; Kalinkevichet, O. Effect of ultrasound treatment on chitosan-silver nanoparticles antimicrobial activity. In Proceedings of the 2018 IEEE 8th International Conference Nanomaterials: Application & Properties (NAP), Zatoka, Ukraine, 9–14 September 2018; IEEE: Piscataway, NJ, USA, 2018; pp. 1–4. [CrossRef]
43. Sohail, Y.; Liaquat, A.; Zafar, M.F.; Ul-Haq, N. Impedance spectroscopy and investigation of conduction mechanism in reduced graphene/CuFe2O4 nanocomposites. *Appl. Phys. A* **2021**, *127*, 423. [CrossRef]
44. Matsuura, K.; Kuboyama, K.; Ougizawa, T. Effect of tacticity of poly (methyl methacrylate) on interfacial region with silica in polymer nanocomposite. *Polym. Eng. Sci.* **2021**, *61*, 77–84. [CrossRef]
45. Abutalib, M.M.; Rajeh, A. Influence of Fe_3O_4 nanoparticles on the optical, magnetic and electrical properties of PMMA/PEO composites: Combined FT-IR/DFT for electrochemical applications. *J. Organomet. Chem.* **2020**, *920*, 121348. [CrossRef]
46. Alghunaim, N.S. In situ synthesis and investigation poly (methyl methacrylate)/polycarbonate nanocomposites incorporated with copper oxide nanoparticles. *Results Phys.* **2020**, *19*, 103368. [CrossRef]
47. Abutalib, M.M. Insights into the structural, optical, thermal, dielectric, and electrical properties of PMMA/PANI loaded with graphene oxide nanoparticles. *Phys. B Condens. Matter* **2019**, *29*, 55219. [CrossRef]
48. Nakanishi, E.Y.; Palacios, J.H.; Godbout, S.; Fournel, S. Interaction between Biofilm Formation, Surface Material and Cleanability Considering Different Materials Used in Pig Facilities—An Overview. *Sustainability* **2021**, *13*, 5836. [CrossRef]
49. Tarrío-Saavedra, J.; López-Beceiro, J.; Naya, S.; Francisco-Fernández, M.; Artiaga, R. Simulation study for generalized logistic function in thermal data modeling. *J. Therm. Anal. Calorim.* **2014**, *118*, 1253–1268. [CrossRef]
50. Wekwejt, M.; Chen, S.; Kaczmarek-Szczepańska, B.; Nadolska, M.; Łukowicz, K.; Pałubicka, A.; Zieliński, A. Nanosilver-loaded PMMA bone cement doped with different bioactive glasses–evaluation of cytocompatibility, antibacterial activity, and mechanical properties. *Biomater. Sci.* **2021**, *9*, 3112–3126. [CrossRef]
51. Giti, R.; Zomorodian, K.; Firouzmandi, M.; Zareshahrabadi, Z.; Rahmannasab, S. Antimicrobial activity of thermocycled polymethyl methacrylate resin reinforced with titanium dioxide and copper oxide nanoparticles. *Int. J. Dent.* **2021**, *2021*, 6690806. [CrossRef]
52. Li, Z.P.; You, S.; Mao, R.; Xiang, J.; Deng, A.C.H.; Shen, J.; Qi, X. Architecting polyelectrolyte hydrogels with Cu-assisted polydopamine nanoparticles for photothermal antibacterial therapy. *Mater. Today Bio* **2022**, *15*, 100264. [CrossRef]
53. Hassanzadeh-Afruzi, F.; Amiri-Khamakani, Z.; Bahrami, S.; Reza Ahghari, M.; Maleki, A. Assessment of catalytic and antibacterial activity of biocompatible agar supported ZnS/$CuFe_2O_4$ magnetic nanotubes. *Sci. Rep.* **2022**, *12*, 4503. [CrossRef] [PubMed]
54. Gheidari, D.; Mehrdad, M.; Maleki, S.; Hosseinic, S. Synthesis and potent antimicrobial activity of $CoFe_2O_4$ nanoparticles under visible light. *Heliyon* **2020**, *6*, e05058. [CrossRef] [PubMed]